RESEARCH ARTICLE | JANUARY 09 2025

Size-dependent phase change in energy storage materials: Comparing the impact of solid-state wetting and of coherency stress

Yong Li ; Jörg Weissmüller

J. Chem. Phys. 162, 024704 (2025)
https://doi.org/10.1063/5.0247515

The Journal of Chemical Physics
ARTICLE
pubs.aip.org/aip/jcp

Size-dependent phase change in energy storage materials: Comparing the impact of solid-state wetting and of coherency stress

Cite as: J. Chem. Phys. 162, 024704 (2025); doi: 10.1063/5.0247515
Submitted: 7 November 2024 • Accepted: 23 December 2024 •
Published Online: 9 January 2025

Yong Li[1] and **Jörg Weissmüller**[1,2,a)]

AFFILIATIONS

[1] Institute of Hydrogen Technology, Helmholtz-Zentrum Hereon, Geesthacht, Germany
[2] Institute of Materials Physics and Technology, Hamburg University of Technology, Hamburg, Germany

[a)] **Author to whom correspondence should be addressed:** weissmueller@tuhh.de

ABSTRACT

Coherent phase transformations in interstitial solid solutions or intercalation compounds with a miscibility gap are of practical relevance for energy storage materials and specifically for metal hydride or lithium-ion compound nanoparticles. Different conclusions on the size-dependence of the transformation conditions are reached by modeling or theory focusing on the impact of either one (internal, solid-state-) critical-point wetting of the nanoparticle surface or coherency constraints from solute-saturated surface layers. We report a hybrid numerical approach, combining atomistic grand canonical Monte Carlo simulation with a continuum mechanics analysis of coherency stress and modeling simultaneously wetting and mechanical constraints. When the ratio between chemical and misfit-strain-related contributions to the solute-solute interaction energy takes values realistic for interstitial solutions—which are typical for energy storage materials—we find that the impact of solid-state wetting is weak and that of coherency stress is dominant. Specifically, mechanical interaction can act to reduce the phase transformation hysteresis at small system size, and it can make the solid more binding for solute, thereby reducing the "plateau" chemical potential at phase coexistence. We present equations for the impact of coherency stress on the size-dependence of upper consolute temperature, plateau chemical potential, and charging/discharging hysteresis.

I. INTRODUCTION

Important energy storage scenarios exploit the reversible insertion and extraction of interstitial solute species, such as hydrogen or lithium, in small particles of a crystalline host substance.[1,2] As a general rule, solute atoms in interstitial solutions or intercalation compounds generate misfit strain in the host crystal lattice. Misfit strain contributes an effectively attractive term to the net (chemical and mechanical) solute–solute interaction energy; this term promotes a miscibility gap in the alloy phase diagram.[3] Rapid solute exchange—which can be attractive in technological scenarios—favors the retention of crystalline coherency during phase change.[4,5] Rapid exchange is promoted by nanoscale particle size, and the enhanced role of surfaces at small size will typically introduce a size-dependence into the alloy phase diagram.[6–18] Size-dependent coherent phase transformations are the subject of the present study.

The simplest analysis of phase equilibrium can be based on free energy density functions that depend on the local solute fraction and that may typically be evaluated at constant and uniform temperature and pressure. One of the corrections to that notion originates in Cahn–Hilliard type chemical gradient energy terms—the local free energy density at a given position depends significantly on the solute fraction in regions of the crystal separated by one or more interatomic spacings.[19] The second correction comes from long-range elastic interactions, which are an immediate consequence of the misfit strain. Elastic interactions have a profound influence on the conditions for and the mechanism of coherent phase transformations.[3,4,17,20–23] Their consequences depend strongly on the dimensionality, the shape, and the size of the host crystal.[18,24,25]

Nonlocal interactions are particularly relevant for the phase-change when surfaces act as sources of heterogeneity and when particles are small with a significant surface-to-volume ratio. Specifically, solid solutions can exhibit surface layers that are strongly enriched in solute; this is exemplified by observations of electrochemical underpotential deposition of H on transition metal surfaces[26] or by implications of density functional theory (DFT) studies of Li segregation to the surface of Li-ion battery cathode materials.[27] By virtue of the nonlocal interactions, the surfaces then bias the entire system toward the more concentrated phase, reducing the driving force required for initiating the phase change in the bulk. Gradient-energy terms may contribute to this reduction[9,28,29] and may even initiate the phase change through a critical-point wetting transition[30] underneath the surface of the solid. Wetting has been proposed as controlling the phase change onset in $LiFePO_4$.[27,31] Yet, it has been pointed out that the coherency stress may have a substantial impact[6,14,15,32] and may be the dominant mechanism by which solute-enriched surface layers affect the phase change in energy storage particles.[18]

While the impact of each, chemical gradient energy or elastic interactions, on phase change in small coherent systems has been studied in isolation, it is not understood how the two terms cooperate or compete in affecting coherent phase change if—as one must assume—they are simultaneously active.[18] Here, we explore this question. Investigating a finite-size open system that undergoes a coherent phase transformation while it exchanges solute with a reservoir, we aim to identify the most fundamentally relevant materials parameters and to study qualitatively their role in affecting the phenomenology. With that in mind, our study focuses on the simplest possible scenario and specifically on constitutive behavior with the minimum amount of required material parameters.

The study is based on an atomistic Monte Carlo scheme that inherently embodies the action of gradient energy and which we adapt to incorporate elastic interactions for a simple but relevant geometry. Different relative magnitudes of chemical bond energy and misfit strain energy are explored.

II. PHENOMENOLOGICAL APPROACH

A. Contributions to the bulk free energy

Our phenomenological description considers a finite-sized solid body B in the absence of external load. We take B as a linear elastic interstitial solid solution on a single-crystal lattice with a constant amount of matrix component and, therefore, a constant amount N_0 of identical sites for interstitials. We focus initially on bulk behavior, ignoring surface effects.

We explore scenarios where B exchanges solute at equilibrium with an external reservoir R at chemical potential μ^{R}. In experiments with R, a gas or electrolyte, the effective value of μ^{R} is controlled via the partial pressure or the electrode potential, respectively. The thermodynamic potential of B that is minimized at equilibrium is here a grand canonical potential, $\mathcal{O}^{\mathsf{B}} = \mathcal{G}^{\mathsf{B}} - \mu^{\mathsf{R}} N$, with $\mathcal{G}^{\mathsf{B}}$ and N the net free energy and the net solute content of B, respectively.

We approximate $\mathcal{G}^{\mathsf{B}}$ by the volume integral over a local free energy density, Ψ, and we take $\Psi = \rho_0 g$, the product of a uniform site density ρ_0 and a molar free energy g. We decompose g into additive terms[3,33] accounting separately for the chemical bond energy or enthalpy (there are, in general, mixed mechanical boundary conditions) $h_{\rm chm}$, the misfit strain energy $h_{\rm mft}$, the coherency strain energy $h_{\rm coh}$ and a contribution, $-Ts_{\rm mix}$, from the entropy of mixing,

$$g = h_{\rm chm} + h_{\rm mft} + h_{\rm coh} - Ts_{\rm mix}, \tag{1}$$

where T is the temperature. Each of these contributions will now be discussed.

B. Chemical bond energy and entropy

The net bond energy, $H_{\rm chm}$, is taken as the sum over all unlike neighbor bonds, each with the bond energy ϵ. This is embodied in the expression

$$H_{\rm chm} = \frac{1}{2}\epsilon \sum_{nn} |o_i - o_j|, \tag{2}$$

with the o the occupancies, 0 or 1 for empty or occupied interstitial sites, respectively, and with the summation carried over all nearest-neighbor pairs. The factor $1/2$ corrects for double-counting of neighbor pairs ij, ji. For attractive solute–solute interactions that result in a miscibility gap, it is required that $\epsilon > 0$.

The bond-counting model's equilibrium configuration can feature significant chemical short-range order; a closed-form equation of state accounting for this effect is not available.[34] Our Monte Carlo scheme (see below) implements this scenario numerically.

As a benchmark, we also consider the regular solution (Ref. 34, Sec. 6.23) as an approximation ignoring chemical short-range order and assuming, instead, a random distribution of the solute over the lattice sites. Then, in a homogenized continuum approximation with x the local solute fraction (fraction of occupied interstitial sites), the local molar entropy of mixing is

$$s_{\rm mix}(x) = -R[x \ln x + (1-x)\ln(1-x)], \tag{3}$$

with R the gas constant.

Except for a solute-matrix interaction term that is linear in x and that will not affect the phenomenology of phase change, the local molar energy in the stress-free solid is[19,35]

$$h_{\rm chm}(x) = \omega_{\rm chm}\left[x(1-x) + \lambda^2\left(\frac{1}{2} - x\right)\nabla^2 x\right], \tag{4}$$

where $\omega_{\rm chm}$ is the chemical part of the solute–solute interaction parameter, in other words, that part which—in the atomistic approach of Eq. (2)—is modeled by the near-neighbor bonds. Ignoring the solute-matrix interaction term means shifting the solute chemical potential μ of all states by a constant; this has the same effect as changing the definition of the reference state for μ.

Bond counting shows that

$$\omega_{\rm chm} = z_0 \epsilon \mathcal{N}_{\rm A}, \tag{5}$$

with $\mathcal{N}_{\rm A}$ Avogadro's number and z_0 the nearest-neighbor coordination number of the crystal lattice. Furthermore, the effective interaction distance λ scales with the nearest-neighbor distance, $r_{\rm NN}$, as $\lambda = r_{\rm NN}/\sqrt{3}$.[19]

In Eq. (4), the term containing the Laplacian $\nabla^2 x$ accounts, in lowest order, for nonlocal interactions in the bond-counting model.[19] When phenomena at the outer surface can be neglected, it can be beneficial to convert this term to one depending on the gradient square, $(\nabla x)^2$, of the composition by applying the divergence theorem;[19] that representation is commonly used in phase-field simulation. The composition-gradient contribution to the local free energy density Ψ is then $\Psi_{\text{grd}} = \frac{1}{2}\kappa(\nabla x)^2$ with κ the gradient energy coefficient and $\kappa = \frac{1}{2}\rho_0 \omega_{\text{chm}} \lambda^2$. For reference in the discussion in Sec V, we here retain the natural, $\nabla^2 x$-based expression.

C. Misfit and coherency strain energies

We define strain relative to the stress-free solid at $x = 0$, and we refer stress as well as all densities to referential (Lagrangian) coordinates. In this frame, we take the solute to cause an isotropic and linear dilatation of the crystal lattice, so that the macroscopic strain tensor $\mathbf{E}$ in the stress-free state relates to x by

$$\mathbf{E} = \eta \mathbf{U} x, \tag{6}$$

with $\mathbf{U}$ the unit tensor in 3D and η a concentration-strain coupling constant, independent of x.

We also limit our consideration to linear and isotropic elasticity. For a uniform solid solution, one then has the molar misfit strain energy[3,36]

$$h_{\text{mft}}(x) = Ax(1 - x), \tag{7}$$

with the Eshelby parameter

$$A = \frac{Y \Omega \eta^2}{1 - \nu}, \tag{8}$$

where Y is the Young's modulus, ν is the Poisson's ratio, and $\Omega = \rho_0^{-1}$ is the molar volume of the interstitial sites.

When the composition is nonuniform, there will generally be long-range stresses that imply the additional "coherency" strain energy h_{coh}. We here consider this quantity for the special case of a plate of constant thickness, infinitely extended in the plane, and fully coherent; compositional variations are restricted to 1D in the thickness direction.[18] The coherency then implies that the in-plane lattice parameter is uniform, independent of the local composition. Then[20]

$$h_{\text{coh}} = A(x - \bar{x})^2, \tag{9}$$

with $\bar{x}$ the mean solute fraction in the plate.

D. Net free energy of the uniform solid solution

Let us first consider a regular solution of uniform x and of constant and uniform pressure. The equation of state for the free energy, here $\widetilde{g}_{\text{P}}$, can then be written as[37]

$$\begin{aligned} \widetilde{g}_{\text{P}}(T, x) &= h_{\text{chm}}(x) + h_{\text{mft}}(x) - T s_{\text{mix}}(x) = \omega_{\text{P}} x(1 - x) \\ &\quad + RT[x \ln x + (1 - x) \ln(1 - x)], \end{aligned} \tag{10}$$

with

$$\omega_{\text{P}} = \omega_{\text{chm}} + A, \tag{11}$$

the total solute–solute interaction parameter; it is this interaction term that applies at constant pressure, in the absence of coherency stress.

Equation (10) is invariant upon $x \to 1 - x$. Since this symmetry also applies to the compositions of the coexisting phases at equilibrium, the associated "plateau" chemical potential must satisfy $\mu^{\text{pla}} = 0$. This refers to phase coexistence at equilibrium, either within a single, incoherent two-phase particle or in an ensemble of single-phase particles sampling the two phases. The μ^{pla} value determines the working partial pressure (for the example of a hydrogen storage material) or the electrode potential (for the example of a battery electrode) in the constant-potential, two-phase region.

For reference below, we summarize selected properties of regular solutions, leaving ω arbitrary so that the results can be applied to various scenarios. Here, the equation of state for the molar free energy is[19]

$$\widetilde{g}(\omega, T, x) = \omega x(1 - x) + RT[x \ln x + (1 - x) \ln(1 - x)],$$

and the chemical potential for interstitials, $\mu = \mathrm{d}g/\mathrm{d}x|_T$, obeys

$$\widetilde{\mu}^{\text{rs}}(\omega, T, x) = \omega(1 - 2x) + RT \ln \frac{x}{1 - x}. \tag{12}$$

The binodals (equilibrium phase coexistence lines in the alloy phase diagram) are here obtained by setting $\mu = 0$ and solving for the temperature. The binodal temperature and composition are then related by (Ref. 34, Sec. 6.23)

$$\widetilde{T}^{\text{bin}}(\omega) = -\frac{\omega}{R} \frac{1 - 2x}{\ln \frac{x}{1 - x}}. \tag{13}$$

Setting $\mathrm{d}\mu/\mathrm{d}x = 0$ provides the spinodal line as

$$\widetilde{T}^{\text{spi}}(\omega) = \frac{2\omega}{R} x(1 - x). \tag{14}$$

Binodal and spinodal of the regular solution meet at composition $x = 1/2$ and upper consolute temperature,

$$\widetilde{T}^{\text{C}}(\omega) = \frac{\omega}{2R}. \tag{15}$$

For the incoherent system and phase coexistence at constant pressure, the upper consolute temperature is $T_{\text{P}}^{\text{C}} = \widetilde{T}^{\text{C}}(\omega_{\text{P}})$. It is often convenient to parameterize T in terms of the dimensionless temperature parameter

$$\tau = T/T_{\text{P}}^{\text{C}} = T/\widetilde{T}^{\text{C}}(\omega_{\text{P}}), \tag{16}$$

and this is here performed in all figures.

The chemical potential hysteresis, $\Delta\mu^{\text{hys}}$, is the difference between the μ for the transformation onsets during charging and discharging (Fig. 1). That difference contributes to the irreversible energy loss during the charging/discharging cycle and, thereby, to the efficiency of a storage device. The maximum value of $\Delta\mu^{\text{hys}}$ is found when the open system becomes unstable at its spinodals; then, analysis of Eq. (12) shows that

$$\widetilde{\Delta\mu}^{\text{hys}}(\omega) = 2\omega\left(\sqrt{1 - \tau_\omega} - \tau_\omega \operatorname{arctanh}\sqrt{1 - \tau_\omega}\right), \tag{17}$$

where $\tau_\omega = T/\widetilde{T}^{\text{C}}(\omega)$. It is readily verified that, for $\tau_\omega \gtrsim 0.5$, Eq. (17) is well approximated by $\Delta\mu^{\text{hys}}(\omega) \approx \frac{4}{3}\ \omega\ (1 - \tau_\omega)^{3/2}$.

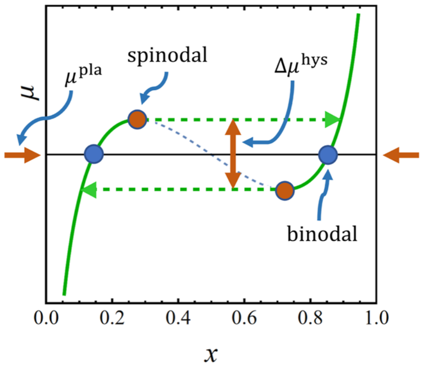

FIG. 1. Schematics illustrating chemical potential isotherm and hysteresis. Labels indicate the plateau chemical potential value $\mu^{\rm pla}$ as well as the binodal and spinodal points. Green dashed horizontal arrows: phase change by instability at the chemical spinodal; solid vertical arrow: the associated chemical potential hysteresis $\Delta\mu^{\rm hys}$.

E. Solution with a 1D composition gradient

Next, we include the coherency strain energy for the plate with a 1D composition gradient (Sec. II C), adding Eq. (9) to Eq. (10). By then taking the variational x-derivative (Ref. 3, Sec. 4.1.1),[29,38] one finds the solute chemical potential at

$$\mu_{\rm coh} = \omega_{\rm chm}\left(1 - 2x - 2\lambda^2 x''\right) + RT\,\ln\frac{x}{1-x} + A(1 - 2\bar{x}). \tag{18}$$

In the special case of uniform composition, we have $x = \bar{x}$ and $x'' = 0$ everywhere, and with Eqs. (11) and (12), one then finds $\mu^{\rm uniform}_{\rm coh} = \tilde{\mu}^{\rm rs}(\omega_{\rm P}, \bar{x})$.

Equation (18) illustrates the impact of coherency on the equilibrium in configurations with a 1D composition gradient.[18] The elastic interaction affects the chemical potential only through the mean composition $\bar{x}$, not through the local composition x. In a closed system, where $\bar{x}$ is a constant, the elastic interactions will then not contribute to the driving forces for phase separation. In other words, the Bitter–Crum theorem[3,18] applies, and the misfit strain energy contribution to the local solute–solute interaction energy is effectively switched off. Consequently, the x-dependence here scales only with $\omega_{\rm chm}$. This will reduce the upper consolute temperature of the miscibility gap and depress both the binodals and the spinodals. This situation is familiar in the context of coherent spinodal decomposition, which exemplifies coherent 1D composition modulation; the depression of the coherent spinodal in infinitely extended solids is well established.[20] In finite-sized systems, the depression of $T^{\rm C}$ has been shown to depend on the size and shape of the system.[6,18,24,25,39]

F. Size dependence due to coherency stress

With attention to finite-sized systems, we here admit that the solute–solvent interaction at the surface may differ from that in the bulk. For simplicity and to avoid introducing additional materials parameters, we restrict attention to the limiting case of a large, negative enthalpy of segregation in all sites of superficial layers L of thickness t at each surface. The layers are then "inert," saturated in solute at solute fraction $x^{\mathsf{L}} = 1$, in the entire range of μ that is of interest to the bulk phase transformation. Considering again a plate of constant overall thickness d, we take the central bulk, of thickness $d - 2t$, as occupied by the uniform active system A that is the subject proper of the analysis.

In the coherent plate, the uniform in-plane lattice parameter depends on the mean (averaging over both the inert layers and the active bulk) solute fraction. Specifically, this fixes the in-plane lattice parameter in A at a value that exceeds the local stress-free lattice parameter, resulting in a tensile stress, the magnitude of which depends on the local solute fraction.[18] Tensile bulk stress, induced by solute-enriched interfacial layers, has been demonstrated in experiments on nanoscale Pd-H.[40] A compressive stress in L compensates the tensile stress in A. In a phenomenological description of the surface as a 2D manifold, the stress state in L would be described by the surface stress.[41] The stress state in A exemplifies a surface-induced bulk stress, as embodied in the generalized capillary equation for solids.[42]

An approximate analysis of the present scenario emerges when the gradient interaction in Eq. (18) is ignored. At equilibrium, the solute fraction x must then be uniform in A and

$$\bar{x} = x + \frac{2}{\xi}\left(x^{\mathsf{L}} - x\right), \tag{19}$$

with $\xi = d/t$ a dimensionless plate thickness parameter. Substituting $\bar{x}$ in Eq. (18) with Eq. (19) and comparing the result with Eq. (12), one finds that $\mu = \tilde{\mu}^{\rm rs}(\omega_{\rm plate}, x) + \Delta\mu_{\rm plate}$, with the solute–solute interaction parameter

$$\omega_{\rm plate} = \omega_{\rm P} - \frac{2A}{\xi}, \tag{20}$$

and with the constant additive term

$$\Delta\mu_{\rm plate} = \frac{2A}{\xi}\left(1 - 2x^{\mathsf{L}}\right). \tag{21}$$

The same results were obtained in Ref. 18 from a different derivation.

Equations (20) and (21) show that the values of both ω and $\mu^{\rm pla}$ decrease with decreasing size. This embodies weaker binding of solute by other solute and stronger binding of solute by the matrix. The solute–solute interaction is weakened since the coherency constraints diminish the composition-induced strain, thereby reducing the elastic interaction strength. The solute-matrix binding is strengthened since the solute, as a center of dilatation, is more readily alloyed into the pre-expanded (tensile stress) lattice sites.

Consistent with Eq. (15), the miscibility gap here closes at the temperature

$$T^{\rm C}_{\rm plate} = T^{\rm C}_{\rm P} - \frac{A}{R\,\xi}, \tag{22}$$

independent of x^{L}.

As adding the constant $\Delta\mu_{\rm plate}$ to μ does not affect the composition at phase coexistence, we expect the binodals for the bulk to agree with those of the extended system. Entering the corresponding solute fractions into Eq. (12) would give $\mu = 0$, and accounting for the additional term of Eq. (21) with $x^{\mathrm{L}} = 1$, one obtains the plateau value of μ at

$$\mu^{\mathrm{pla}} = \Delta\mu_{\mathrm{plate}}\big|_{x^{\mathrm{L}}=1} = -\frac{2A}{\xi}. \qquad (23)$$

Finally, the approximate form (see Sec. II D) of Eq. (17) implies here for the hysteresis

$$\Delta\mu^{\mathrm{hys}}_{\mathrm{plate}} \approx \frac{4}{3}\,\omega_{\mathrm{plate}}\left(1 - \frac{T}{T^{\mathrm{C}}_{\mathrm{plate}}}\right)^{3/2}, \qquad (24)$$

where ω_{plate} and $T^{\mathrm{C}}_{\mathrm{plate}}$ are given by Eqs. (20) and (22), respectively.

Inert layers will also interact with the active bulk through chemical gradient energy contributions. Those contributions are embodied in our atomistic description and explored in the numerical part of our study.

G. Exemplary materials parameters

We aim for materials parameter values that are qualitatively consistent with a typical interstitial metal hydride and, to this end, use data matched to the Pd-H system.[43,44] The lattice of interstitial sites is face-centered cubic (fcc) with lattice parameter $a_0 = 389.0$ pm,[45] $z_0 = 12$ nearest neighbors, and four interstitial sites per unit cell. The incoherent upper consolute temperature is $T^{\mathrm{C}}_{\mathrm{P}} = 566\mathrm{K}$,[46,47] the (polycrystalline) Young's modulus is $Y = 120$ GPa, Poisson's ratio is $\nu = 0.396$,[48] and the concentration-strain coefficient is $\eta = 0.060$.[49–51]

Based on the $T^{\mathrm{C}}_{\mathrm{P}}$ value and Eq. (15), one finds $\omega_{\mathrm{P}} = 9.41$ kJ/mole for Pd-H. Furthermore, the elastic parameters imply that $A = 6.17$ kJ/mole, hence $\omega_{\mathrm{chm}} = \omega_{\mathrm{P}} - A = 3.24$ kJ/mole.

As an important simplification, we find that the above-mentioned parameters enter our computation through a single quantity, which we refer to as the misfit strength parameter, $\mathbb{Q}$. It is defined as

$$\mathbb{Q} = \frac{A}{\omega_{\mathrm{P}}} = \frac{A}{\omega_{\mathrm{chm}} + A}, \qquad (25)$$

and is closely analogous to the atomic-scale "elastic misfit parameter" of Ref. 52. As $\mathbb{Q} = 0.656$ for Pd-H, about two-thirds of the attractive solute–solute interactions are here from the misfit strain, and only about one-third is from the chemical bonds.

Strong enrichment of H at Pd surfaces, as supposed in our "inert layer" scenarios, is well documented by studies of underpotential deposition.[26] The experiment suggests a thickness $t = 1.0$ nm of H-rich layers at surfaces[15] or grain boundaries[6,40,53] in Pd-H; this corresponds to 4–5 dense-packed crystal planes.

On top of Pd-H, analogous data for (Li)FePO$_4$—as an important lithium-ion battery electrode material—are of interest. The estimates provided in Sec. S1 of the supplementary material here suggest $\mathbb{Q} = 0.64$. This is quite similar to Pd-H and qualifies the results of our numerical analysis as equally relevant for the metal hydride and the lithium-ion compound.

III. ATOMISTIC APPROACH

A. Implementation in the atomistic Monte Carlo study

For identifying states of local equilibrium and thermodynamic averages of their composition fields in an atomistic approach, we used a grand canonical Metropolis Monte Carlo (gcMMC) simulation[54,55] on a rigid, 3D fcc lattice with nearest-neighbor bonds. The code is based on our implementation of kinetic Monte Carlo simulation of alloy corrosion.[56–58]

The model's restriction to a rigid lattice prevents the implementation of mechanical interactions for general composition fields. Yet, if the system is either uniform or exhibits composition gradients along only one dimension, then Eq. (18) applies, and the mechanical interactions enter simply through a shift of the equilibrium chemical potential that depends on the current value of the mean solute fraction, $\Delta\mu = A(1 - 2\bar{x})$. As compared to the uniform grand-canonical system, the work of exchanging the amount δN of solute with the reservoir is then modified by $\Delta\mu\delta N$. Therefore, one may replace the chemical potential, μ^{R}, in the reservoir with

$$\mu_{\mathrm{eff}} = \mu^{\mathrm{R}} - A(1 - 2\bar{x}), \qquad (26)$$

when computing event probabilities. For 1D gradients, this affords inclusion of mechanical interaction in the simulation, even though site displacements are not explicitly implemented.

The gcMMC elementary event is swapping the occupancy of a site between the two possible values, 0 or 1, for vacant or solute-occupied. Repeatedly, a site is selected at random, and the swap is executed with probability $\hat{p}$. When the swap changes the system's energy by $\Delta\hat{H}$ and its net number of solute atoms by $\delta\hat{N} = \pm 1$, and when the reservoir is at chemical potential $\hat{\mu}^{\mathrm{R}}$, then $\hat{p}$ may be taken as[55,59]

$$\hat{p} = \mathrm{Min}\left[1,\ \exp\left(-\frac{\Delta\hat{H} - \delta\hat{N}\hat{\mu}^{\mathrm{R}}\ \mathcal{N}_{\mathrm{A}}^{-1}}{kT}\right)\right], \qquad (27)$$

where $\mathcal{N}_{\mathrm{A}}$ and k represent Avogadro's number and Boltzmann's constant, respectively, and the term $\delta\hat{N}\hat{\mu}^{\mathrm{R}}$ accounts for the work of exchanging solute between the system and reservoir.

Specifically for the present study, site j is initially at occupancy o_j, and it has z^{unl}_j unlike neighbor bonds. The changes in the amount of solute and in the net number of unlike neighbor bonds are then $\delta N_j = 1 - 2o_j$ and $\Delta z^{\mathrm{unl}}_j = z_0 - 2z^{\mathrm{unl}}_j$, respectively. The net bond energy changes by $\Delta H_j = \epsilon\Delta z^{\mathrm{unl}}_j$. Accounting for the mechanics-related work and Eq. (26), we may replace $\hat{\mu}^{\mathrm{R}}$ in Eq. (27) with μ_{eff}. The swapping probability, p_j, for site j is then

$$p_j = \mathrm{Min}\left[1,\ \exp\left(-\frac{\Delta H_j - (1 - 2o_j)\mu_{\mathrm{eff}}\ \mathcal{N}_{\mathrm{A}}^{-1}}{kT}\right)\right]. \qquad (28)$$

Evaluating the system evolution by Eq. (28) amounts to searching for states that statistically minimize a grand canonical potential. For a given system, T and μ^{R} are the variables through which the simulation explores the phase behavior.

As outlined in Sec. S2, Eq. (28) is implemented, in our code, in terms of dimensionless parameters. The materials parameters, and specifically the solute–solute interaction energies, enter this implementation through a single quantity, namely the misfit strength parameter $\mathbb{Q}$, which completely parameterizes the relevant materials characteristics. As summarized in Table I, simulations used $\mathbb{Q} = 0$ for scenarios with $\omega_{\mathrm{P}} = \omega_{\mathrm{chm}}$ (no misfit strain) and $\mathbb{Q} = 0.656$ (see Sec. II G) for scenarios that do account for size misfit.

Equilibrium states were identified and analyzed as follows. The net solute fraction, $x_{\mathrm{tot}} = N/N_0$, with N the net amount of solute in the active simulation volume A and N_0 the amount of interstitial sites in A, was evaluated every $50 \times N_0$ successful swap events. A state of equilibrium was determined when the change in x_{tot} between two successive evaluations was less than 10^{-4}. The mean composition in each crystal plane parallel to the surface was then computed every N_0 successful swap events. This was repeated 50 times successively, and the equilibrated composition profile was calculated by averaging the 50 composition values of each crystal plane. The equilibrated compositions of bulk, x_{blk}, and net, x_{tot}, as well as the superficial excess in solute, were determined based on this averaged composition profile. For scenarios with free surfaces or inert layers, crystal planes with sufficiently small composition variation relative to their neighboring plane, $\Delta x < 10^{-3}$, were identified as "near-center planes," and x_{blk} was computed as the average composition in that set of planes.

Approximations to the equilibrium phase diagrams were computed by setting μ^{R} to the estimated plateau chemical potential value (Secs. II D and II F) and computing the solute fraction vs temperature. Simulations started at $\tau = 1/3$ and successively scanned up to $\tau = 7/6$ in a discrete step of $\Delta\tau = 0.1/6$, using the previous solution as the starting configuration. To access the dilute and the concentrated binodal, two separate runs used approximations to the dilute and the concentrated phase, respectively, as the initial configurations.

For each scenario, we computed chemical potential isotherms for $0.5 \le \tau \le 0.9$ in steps of 0.1. The computation of each isotherm was initialized with the pure matrix. It then equilibrated successively at stepwise increasing μ up to an upper vertex value and continued by stepping μ back down. Each step started from the configuration at the end of the previous step. The isotherms afforded a verification of the plateau chemical potential estimates and an inspection of hysteresis.

The Gibbs excess, Γ, in solute was determined as

$$\Gamma = \frac{N - N_0\, x_{\mathrm{blk}}}{\mathcal{A}\rho^{\mathsf{S}}}, \tag{29}$$

with $\mathcal{A}$ the total area of surface (both sides of the plate sample) and ρ^{S} the area density of sites in a dense-packed (here, 111-type) crystal plane. This definition provides Γ in units of dense-packed monolayers (ML). The permanently bound solute in the inert layers is not included in our Γ value.

B. Simulation geometry and surface-specific interactions

The geometry under study is a 3D plate-shaped sample with (111) surfaces and {110}- and {112}-type side faces. Periodic boundary conditions apply either in-plane or in all three dimensions. The simulation acts to equilibrate the solute concentration in A, which consists of n^{A} crystal planes. Except for the scenario with $n^{\mathsf{A}} = 18$, all other scenarios had $n^{\mathsf{A}} = 36$ (see Table I). In terms of the interplanar spacings, d_{hkl}, of the side faces, the lateral extensions were $275 d_{110}$ and $146 d_{112}$. There were 80 300 sites in total for each (111) crystal plane, and in total, 2.89×10^6 active sites for the scenarios with $n^{\mathsf{A}} = 36$.

As detailed in Sec. IV A below, some scenarios had A bounded, at each of its two surfaces, by solute-saturated layers L, each comprising n^{L} inert crystal planes. In the code, L is not actually implemented in the form of additional sites. Instead, bond counting for the outermost crystal planes of A here accounts for bonds crossing the $\mathsf{A} - \mathsf{L}$ interface and for $o = 1$ in the layers.

Whether or not layers and bulk interact mechanically by coherency stress is determined by the tracking of $\bar{x}$ for use in Eq. (26). In scenarios with coherency stress, $\bar{x}$ includes all sites and all solute atoms in A and in L, whereas $\bar{x}$ in scenarios without coherency stress accounts exclusively for solute in A.

TABLE I. Listing the scenarios of the numerical study. Columns indicate, successively, the scenario acronym, the presence (Y) or absence (N) of an inert surface layer, the value, $\mathbb{Q}$, of the misfit strength parameter, the solute fraction x^{L} in the inert layers, the number n^{L} of coherent, stiffening crystal planes in each inert layer, the number n^{A} of crystal planes in the active region of the plate, the nature (2D or 3D) of the periodic boundary conditions (pbc), and a comment on the nature of the scenario. Non-applicable table cells show % as entry.

Acronym	Inert layer	$\mathbb{Q}$	x^{L}	n^{L}	n^{A}	pbc	Comment
bchm	%	0	%	%	36	3D	Bulk for reference, chemical interaction only
bmft	%	0.656	%	%	36	3D	Bulk for reference, with misfit
fchm	N	0	%	%	36	2D	Free surface, chemical interaction only
fmft	N	0.656	%	%	36	2D	Free surface, with misfit
ichm	Y	0	1	0	36	2D	Inert layers, chemical interaction only
imft	Y	0.656	1	0	36	2D	Inert layers, misfit, no coherency stress
icoh	Y	0.656	1	4	36	2D	Inert layers, misfit, with coherency stress
icoh-thin	Y	0.656	1	4	18	2D	Inert layers, misfit, with coherency stress, thinner active region

IV. RESULTS FOR THE PHASE-CHANGE BEHAVIOR

A. Model scenarios

As a simple model geometry—incorporating the effects of coherency stress, size, and surfaces—we studied a laterally extended, planar, and crystallographically coherent single-crystal plate, S, of uniform thickness, d, and with uniform bond energy and elastic parameters. Different assumptions were made on the nature of the solute–solute interaction energy and of the bounding surfaces. Table I summarizes the resulting scenarios, and Fig. 2 provides an illustration.

The solute–solute interaction was assumed to be either of exclusively chemical origin or due to a combination of chemical and misfit strain interaction with the misfit strength parameter $\mathbb{Q}$ matched to Pd-H (see Sec. II G). The respective scenarios have acronyms with “chm” or “mft,” respectively.

Reference scenarios explored bulk behavior (acronyms bchm and bmft) by featuring periodic boundary conditions in three dimensions. In all other scenarios, S was bounded, in each out-of-plane direction, by a surface.

In an idealized finite-size scenario [Fig. 2(a)], the surfaces simply truncate the lattice of interstitial sites, reducing the coordination number of near-surface solute but with no further impact on bond energies or stress. We refer to this scenario as “free surface” (acronyms fchm and fmft).

More realistic are scenarios in which a strong enthalpy of segregation fixes the composition in “inert” layers L at $x^{\mathsf{L}} = 1$ (see Sec. II F). For dense-packed surfaces with nearest-neighbor interaction, only the innermost crystal plane of each inert layer forms bonds with the active region of the bulk crystal lattice, and this chemical interaction is independent of the layer thickness t whenever L comprises at least one monolayer. Scenarios ichm and imft [Fig. 2(b)] explored this variant of the inert layer scenario in isolation, excluding the mechanical interaction between layers and bulk. These scenarios naturally include gradient-energy interactions at the interface, thereby admitting a conceivable wetting transition.

The coherency stresses depend—through Eq. (9)—on $\bar{x}$ and, thereby, on the net solute content in L, which scales with t. Scenarios icoh and icoh-thin [Fig. 2(c)] explored the combined impact of cross-interface chemical bonding and of coherency stress for layers with two different thicknesses.

B. Bulk alloy

For verification of the simulation scheme, we started out with studying the uniform bulk phases that emerge when 3D periodic boundary conditions are applied. The temperature-dependent compositions at $\mu^{\mathrm{R}} = 0$, which approximate the binodals, are shown in Fig. 3. For reference, the gray solid line shows the binodals, $T^{\mathrm{bin}}(\omega_{\mathrm{P}})$, of the regular solution, Eq. (13), with solute–solute interaction parameter ω_{P}. Here and throughout this work, the diagrams parameterize the temperature by τ [Eq. (16)], thereby referring the temperature scale to the upper consolute temperature of the incoherent regular solution with the same ω_{P} as the respective simulation scenario.

The squares in Fig. 3(a) represent numerical results for scenario bchm, the solution with no atomic size misfit and, hence, $\omega_{\mathrm{P}} = \omega_{\mathrm{chm}}$. Its upper consolute temperature emerges as $\tau^{\mathrm{C}} = 0.84$. The reduction, compared to the regular solution, and the narrowed miscibility gap are well-known consequences of the chemical

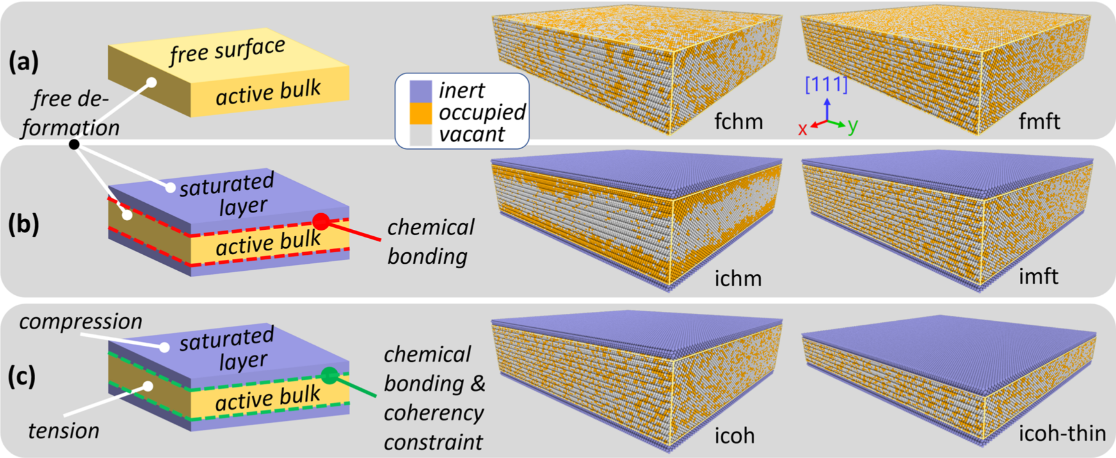

FIG. 2. Schematic representation of the model scenarios, which are plates with periodic boundary conditions in the plane and with surfaces of different nature. Left hand side: Cartoons illustrating elements and boundary conditions; right hand side: renderings of atomic-scale simulation results, showing atoms in cutouts from the laterally much larger simulation box. (a) At free surfaces, the uniform bulk crystal lattice is simply truncated; the surface atoms differ from bulk only by a reduced coordination number. In scenario fchm, the solute–solute interaction is exclusively from chemical bonds, whereas scenario fmft also include mechanical interaction due to atomic size misfit. (b) Scenarios ichm and imft consider the surface of the active bulk in contact with an inert layer, saturated in solute, that interacts with the bulk exclusively through chemical bonds across the bulk-layer interface. Those bonds can promote wetting. The mechanical interaction between layer and bulk is ignored. (c) On top of the through-interface chemical bonds, scenarios icoh (36 crystallographic planes in the active bulk) and icoh-thin (18 planes) also account for coherency stresses between the inert layer and the active bulk. The layer is then strained in compression while the bulk is in tension. Color code for renderings and orientation of the surface normal are indicated.

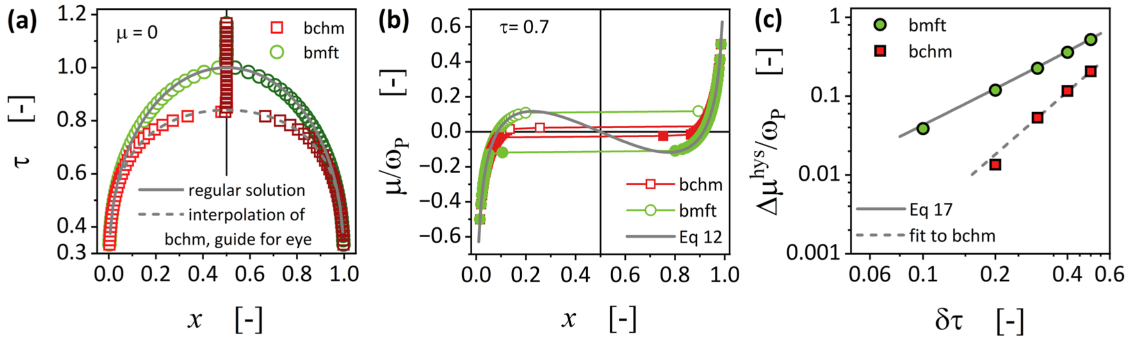

FIG. 3. Simulation results for bulk scenarios with 3D periodic boundary conditions. (a) Solute fraction x at chemical potential $\mu = 0$ vs dimensionless temperature, τ. Red squares and label bchm: Scenario with only chemical interaction; green circles and label bmft: scenario with chemical and misfit interaction, with interaction strength parameter matched to Pd-H. Gray solid line: Regular solution, Eq. (13) with $\omega = \omega_{\mathrm{P}}$. Gray dashed line: Approximate interpolation of the bchm data, used as benchmarks in later figures. (b) Isotherms of chemical potential, μ, normalized to the total solute–solute interaction parameter ω_{P}, vs solute fraction x at reduced temperature $\tau = 0.7$. Symbols as in part (a); the gray line represents the regular solution, Eq. (12) with $\omega = \omega_{\mathrm{P}}$. Open (closed) symbols refer to simulation scanning to increasing (decreasing) μ; lines connect the symbols. (c) Normalized chemical potential hysteresis, $\Delta\mu^{\mathrm{hys}}/\omega_{\mathrm{P}}$, between charging and discharging reactions plotted vs the temperature variable $\delta\tau = 1 - \tau$. Symbols: Numerical results; solid line: theory for spinodal instability of the regular solution, Eq. (17); dashed line: straight-line fit to the bchm data for reference in later figures. Note the excellent agreement for scenario bmft, acknowledging misfit strain energy.

short-range order, which is ignored in the regular solution model (Ref. 34, Sec. 6.24). The dashed line in the graphics is a guide to the eye, marking the bond-counting model's binodal for reference in phase diagrams for other scenarios (see below). For $\tau > \tau^{\mathrm{C}}$, the degeneracy is lifted in favor of a single phase with $x|_{\mu^{\mathrm{R}}=0} = 1/2$ [vertical line in Fig. 3(a)].

Next, we studied the bulk alloy phase diagram for the solution with misfit, scenario bmft. As can be seen in Fig. 3(a), the binodals here follow closely those of the regular solution. That is intuitively right: the chemical short-range order is here expected to be weak, as it arises from the chemical near-neighbor bonding—as opposed to the misfit strain energy—which here makes up only about one third of the solute–solute interaction strength.

Figure 3(b) exemplifies chemical potential isotherms, here at reduced temperature $\tau = 0.7$, for the two above-mentioned scenarios. The figure also shows the regular solution result, Eq. (12). Consistent with the discussion earlier, the bulk scenario with misfit agrees closely with the regular solution isotherm.

It is also significant that the isotherms in Fig. 3(b) can be followed sensibly up to their spinodal points (marked by horizontal tangents); at this point the solution becomes unstable and switches over to the other phase. Specifically for scenario bmft, which acknowledges misfit strain contributions, Fig. 3(c) shows that the full spinodal spread between the charging and discharging transitions is exploited, quite precisely as predicted by Eq. (17). This confirms that phase-change in the potential scan of our gcMMC simulation setup occurs quite near the spinodal instability. Therefore, the behavior of the simulation is empirically consistent with that of open coherent systems in experiment, where a macroscopic energy barrier prevents thermally activated nucleation[4] and where the phase change is initiated, instead, by a continuous switchover instability that acts at the chemical spinodal.[18,23] We may, therefore, compare the hysteresis in the gcMMC isotherms to the theory prediction for hysteresis.

C. Finite-thickness plate with free surfaces

As an additional verification, we investigated the free-surface scenarios, fchm with chemical interaction only and fmft including misfit. Figure 4 displays the results (symbols), along with the bulk regular and bulk bond-counting solutions (gray lines) as benchmarks. The simulation data for the binodals in Fig. 4(a) here take the form of two separate composition values at each temperature, the net solute fraction x_{tot} (closed symbols) and the bulk value x_{blk} (open symbols) that represents the central region of the plate. Both are seen to agree closely with the results from the bulk simulation for the respective scenario. The close agreement between plate and bulk is here also found for the sorption isotherms, Fig. 4(b). The central observation from these scenarios is that the presence of free surfaces affects the equilibrium solute distribution only weakly.

A detailed inspection of the results in Fig. 4(a) reveals a slightly narrowed miscibility gap for the x_{tot} as compared to the x_{blk} values, indicating a weak enrichment of solute at the surface in the dilute phase and depletion in the concentrated phase. The effect is somewhat stronger for the scenario with only chemical interaction. The graph of the Gibbs excess, Γ, in solute for the terminal solutions of Fig. 4(c) confirms this observation. For the chemical-interactions-only simulation, Γ increases throughout the approach to the upper consolute temperature, whereas the simulation with misfit interaction finds Γ at maximum at an intermediate temperature. In each case, the graph is symmetric between excess ($\Gamma > 0$) in the dilute phase and depletion ($\Gamma < 0$) in the concentrated one. This is consistent with the nature of the free surface, which involves no symmetry-breaking interaction term.

The observation of a surface excess may appear surprising, since scenarios fchm and fmft include no surface-specific interaction term. Yet, the observation has a natural explanation in terms of Eq. (5). That equation links the chemical solute–solute interaction parameter to the coordination number, z_0. That quantity is reduced at the surface, a simple consequence of the missing neighbors. The

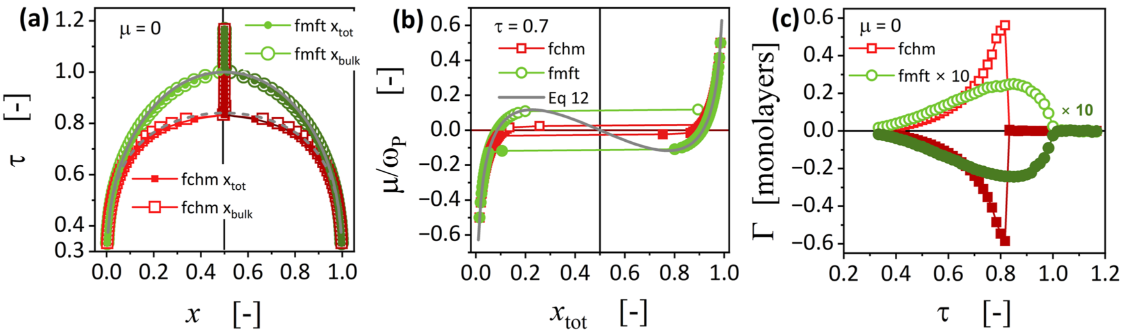

FIG. 4. Simulation results for thin (36 active 111-layers) slabs with free surfaces and 2D in-plane periodic boundary conditions. (a) Solute fraction x at chemical potential $\mu = 0$ vs dimensionless temperature, τ. Red squares and label fchm: Scenario with only chemical interaction; green circles and label fmft: scenario with chemical and misfit interaction, with interaction strength parameter matched to Pd-H. Open symbols: bulk solute fraction x_{blk}; closed symbols: net solute fraction x_{tot}. Gray solid and dashed lines: Bulk regular solution and bulk atomistic model, respectively, as in Fig. 3. Note close agreement with the results for the bulk scenarios. (b) Isotherms of chemical potential, μ, normalized to the total solute–solute interaction parameter ω_P, vs the net solute fraction x_{tot} at reduced temperature $\tau = 0.7$. Symbols as in part (a). Gray line: Regular solution as a benchmark. Open (closed) symbols refer to simulation scanning to increasing (decreasing) μ; lines connect the symbols. (c) Gibbs excess, Γ, in solute vs τ at $\mu = 0$, i.e., for the states represented in part (a). Open symbols and positive values refer to dilute bulk, while closed symbols and negative values refer to concentrated bulk. Note that the fmft graph (with misfit interaction) has been multiplied by 10 for visibility on the same scale as the fchm graph (chemical interaction only).

outermost layer at the surface is thus at a higher homologous temperature, compared to T^C, and so favors local solute fractions closer to 1/2 than the bulk. This leads to a solute-enriched surface in the dilute phase and a solute-depleted surface in the concentrated one, as observed.

Figure 2(a) includes renderings for scenarios fchm and fmft, just before their transformation onsets near the respective τ^C. In agreement with the small Γ values, the solute distribution is essentially uniform along the thickness direction. In scenario fchm, clusters of both species illustrate the substantial short-range order.

D. Inert surface layers coupling by chemical gradient energy

Next, we studied specimens with solute-saturated inert layers, ignoring coherency stress but accounting for chemical bonds between layers and the active bulk.

For scenario ichm, the full squares in Fig. 5(a) show phase coexistence lines at $\mu^R = 0$, plotted vs the net solute fraction, x_{tot}, in the active layer. Sufficiently below T^C, the graph for the concentrated phase coincides with that for bulk. By contrast, the dilute phase shows a substantial net enrichment, implying solute-enriched regions at the surfaces. These regions result from gradient energy terms that tend to shift the solute fraction near the surface of the active bulk toward that, $x = 1$, in the inert layers. As the temperature is increased, the enrichment eventually leads to a phase change to the concentrated phase, well below the bulk T^C. The critical point is here approached along the concentrated binodal, even when the system started out in the dilute phase.

The circular symbols in Fig. 5(a) refer to scenario imft. Here, the dilute and the concentrated phase both move closely along the bulk binodals. The phase transformation is again initiated with a finite downshift from T^C, yet by a substantially smaller shift than in

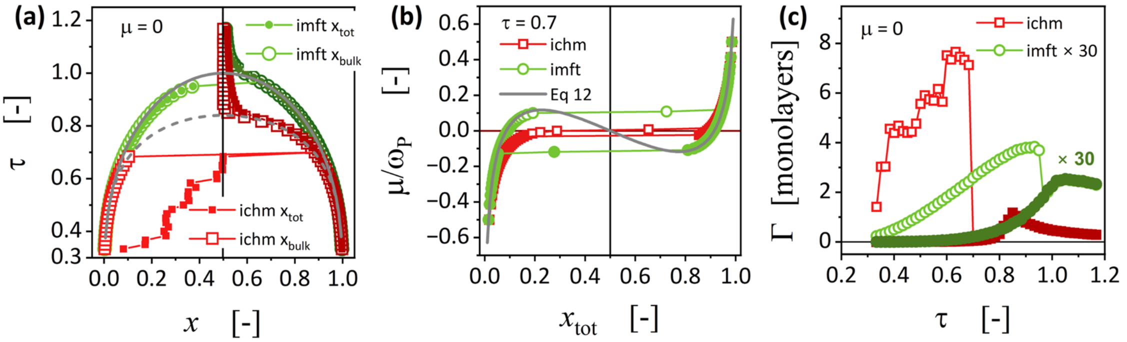

FIG. 5. (a–c) Simulation results for thin (36 active 111-layers) slabs with solute-saturated surface layers that interact with the active bulk via chemical bonds but not via coherency stress. Red squares and label ichm: Scenario with only chemical interaction; green circles and label imft: scenario with chemical and misfit interaction, with interaction strength parameter matched to Pd-H. All other elements as in Fig. 4. In (a), note the restricted temperature range of stability for the dilute phase. In (c), note that the imft graph (with misfit interaction) has been multiplied by 30 for visibility on the same scale as the ichm graph (chemical interaction only).

the chemical-interaction-only scenario. Those observations may be understood as the consequence of the weak gradient energy coefficient in scenario imft. Recall that, in our model, this coefficient scales with the chemical part of the solute–solute interaction energy, which is here only one third of that in scenario ichm.

The chemical potential isotherm of scenario ichm [squares in Fig. 5(b)] is slightly shifted downwards, reflecting the effect of the attractive solute–solute interaction originating in the inert layers and propagating into the active part by virtue of the gradient interaction. Furthermore, the hysteresis is diminished in that scenario. By contrast, the isotherm of scenario imft (circles) agrees closely with that of the respective bulk scenario.

Figure 5(c) shows the temperature variation of Γ for the configurations (at the plateau chemical potential) of Fig. 5(a). Scenario ichm, with the strong chemical bonding, is distinguished by a substantial superficial excess when the matrix phase is dilute. The excess is not noticeable when the matrix phase is concentrated, and it is small and positive in the single phase states above τ^{C}. For a dilute matrix and starting out from low temperature, one initially finds Γ increasing with increasing temperature. As the bulk transitions to the concentrated phase, Γ drops back to a small value. Maximum values of Γ can reach several monolayers. The ichm rendering in Fig. 2(b) illustrates the thick solute-rich region underneath the surfaces of scenario ichm. This is similar to a solid-state critical-point wetting scenario, yet the $\Gamma(\tau)$ function is continuous, with no sign of a wetting transition.

For the imft scenario with misfit, the excess is almost two orders of magnitude smaller than for the ichm scenario with strong chemical interaction. The imft rendering in Fig. 2(b) illustrates that superficial solute enrichment is insubstantial in this scenario. Note that the imft data in Fig. 5(c) have been multiplied by 30 for visibility on the scale of the much larger excess of the ichm scenario.

The central finding from this part of our study is that the interaction between an inert surface layer and the bulk can have a strong effect on the location of the phase-change instability in composition-temperature space. Yet, we also observe that this is restricted to solutions with small misfit strain. When a realistic misfit strength parameter for interstitial solutions is accounted for, the gradient-energy mediated interaction between the solute-enriched surface layer and the bulk is weak, and it causes only a little shift in the phase change behavior.

E. Inert surface layers coupling by coherency stress

The scenarios here again comprise solute-saturated inert layers and their chemical bonds with the bulk. As a distinction to the previous scenarios, they now admit for coherency stress.

Phase coexistence lines are shown in Fig. 6(a) for plates 36 and 18, with active bulk crystal planes thick in scenarios icoh and icoh-thin, respectively, and covered with inert layers comprising an extra four crystal planes at each surface. When comparing the graphs to that of the uniform regular solution, one immediately perceives that the lines for both phases, dilute and concentrated, are substantially displaced to lesser temperature, increasingly so as the plate thickness is decreased.

The sorption isotherms in Fig. 6(b) are displaced to lesser chemical potential, and they exhibit a reduced hysteresis. Here again, the effect increases as the layer thickness is reduced.

Inspection of the $\Gamma(\tau)$ graphs in Fig. 6(c) reveals an extremely small superficial excess in solute, only a small fraction of a crystallographic monolayer. The renderings in Fig. 2(d) confirm the lack of significant superficial solute enrichment in either of the two scenarios. Clearly, the shift of the phase coexistence lines is not due to excess solute near the surface. In other words, the change in the phase coexistence lines is almost exclusively an effect of the coherency stress. That is consistent with the theory in Ref. 18, which predicts a downshift of the critical temperature

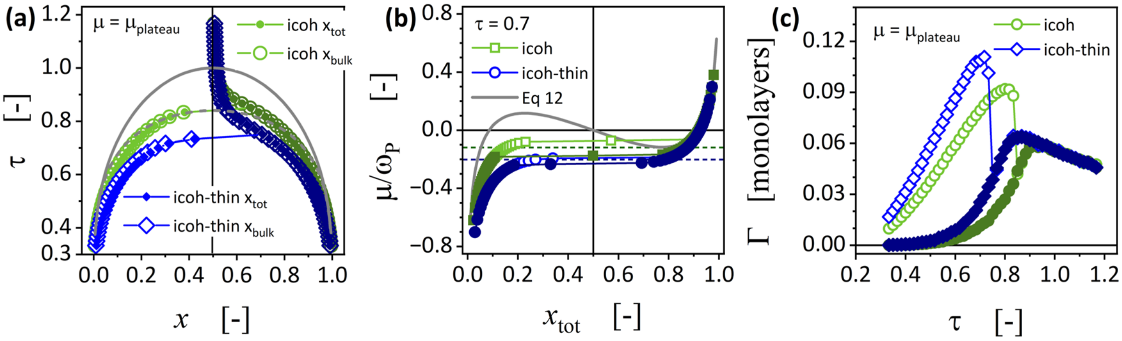

FIG. 6. Simulation results for thin (36 or 18 active 111-layers) slabs with solute-saturated surface layers that interact with the active bulk via chemical bonds and via coherency stress. (a) Solute fraction x at the plateau chemical potential [Eq. (23)] vs dimensionless temperature, τ. Green circles and label icoh: 36 layer thick plate; blue lozenges and label icoh-thin: 18 layer thick plate. Open symbols: bulk solute fraction x_{blk}; closed symbols: net solute fraction x_{tot}. Gray solid and dashed lines: bulk regular solution and bulk atomistic model, respectively, as in Fig. 3. Note the size-dependent shift of phase boundary lines and restricted temperature range of instability for the dilute phase. (b) Isotherms of chemical potential, μ^{R}, normalized to the total solute-solute interaction parameter ω_{P} vs the net solute fraction x_{tot} at reduced temperature $\tau = 0.7$. Symbols as in part (a). Gray line: regular solution as a benchmark; dashed lines: plateau chemical potentials from Eq. (23). Open (closed) symbols refer to simulation scanning to increasing (decreasing) μ^{R}; lines connect the symbols. (c) Gibbs excess, Γ, in solute vs τ at $\mu^{\mathrm{R}} = 0$, i.e., for the states represented in part (a). Open symbols and larger values refer to dilute bulk, while closed symbols and smaller values refer to concentrated parts.

because the coherency stresses reduce the effective solute-solute interaction energy in the bulk.

F. Summary of metrics characterizing the size-dependence

We now compare results, from theory and simulation, for metrics characterizing the size-dependence of the phase change in scenarios with inert surface layers. We start out by summarizing the theory for the impact of coherency stress in a reduced notation. This is obtained by using Eq. (25) to substitute $\mathbb{Q}$ for A in Eqs. (22)–(24). This yields

$$\frac{T^{\mathrm{C}}_{\mathrm{plate}}}{T^{\mathrm{C}}_{\mathrm{P}}} = 1 - \frac{2\mathbb{Q}}{\xi}, \tag{30}$$

$$\frac{\mu^{\mathrm{pla}}_{\mathrm{plate}}}{\omega_{\mathrm{P}}} = -\frac{2\mathbb{Q}}{\xi}, \tag{31}$$

$$\frac{\Delta\mu^{\mathrm{hys}}_{\mathrm{plate}}}{\omega_{\mathrm{P}}} = \frac{4}{3}\left(1 - \frac{2\mathbb{Q}}{\xi}\right)\left(1 + \frac{\xi\,\tau}{2\mathbb{Q} - \xi}\right)^{3/2}, \tag{32}$$

emphasizing again that the misfit strength parameter $\mathbb{Q}$ embodies the relevant material characteristics here.

Figure 7 summarizes the size-dependency of the upper consolute temperature. The open circle labeled fmft represents the free-surface scenario. Scenario imft (the second open circle) differs by the presence of a saturated inert layer that interacts with the outermost active surface layer by chemical gradient energy. This interaction is seen to induce a weak reduction in τ^{C}. The downward shift in τ^{C} is much stronger for the scenarios with coherency stress (closed circles). Here, τ^{C} decreases in proportion to the inverse thickness. The numerical findings agree with Eq. (30), except for an extra depression that is similar in magnitude to that between fmft and imft. This observation is compatible with the notion that the downwards deviation from Eq. (30) reflects the action of the chemical gradient energy at the surface. Additional simulation results, confirming this notion, are shown in the supplementary material, Sec. S3. Therefore, gradient energy has a noticeable contribution to the suppression of τ^{C}, yet the impact of coherency strains is substantially stronger.

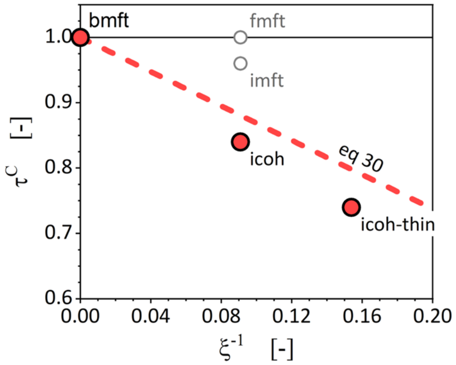

FIG. 7. Size-dependence of upper consolute temperature in samples with coherency stress. Dimensionless upper consulates temperature parameter τ^{C} plotted vs the inverse of the dimensionless thickness parameter ξ. Symbols: simulation; dashed line: Eq. (30). For reference, data points labeled "bmft," "fmft," and "imft" show bulk limit, scenario with free surface, and scenario with inert layer but ignoring coherency stress, respectively.

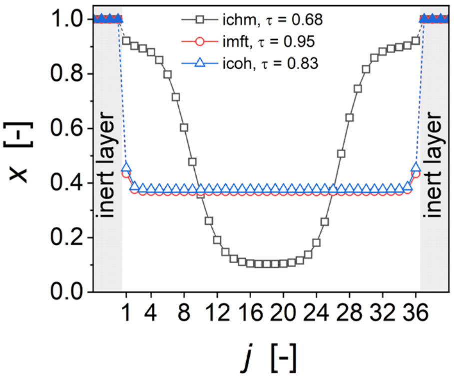

FIG. 8. Composition profiles at the plateau chemical potential and right before the onset of the transformation to the concentrated phase near the upper consolute temperature, τ^{C}. Open symbols: solute fraction x vs the layer number j through the thickness of plates with 36 active layers. Closed symbols and shaded regions: inert layers. Labels indicate scenarios (see Table I) and their τ^{C}.

Figure 8 shows composition profiles, averaged over each active crystal plane, for different inert-layer scenarios in states right before the onset of the transition to the concentrated phase. Thick wetting layers are apparent in scenario ichm, which neglects misfit strain and assumes chemical interaction only. By contrast, the scenarios with misfit have only small solute enrichment near their surfaces. The large concentration jump at the interfaces between the active bulk and the inert layers shows that the action of the gradient energy is here too weak for substantially affecting the composition profile. The observations further emphasize the comparatively weak impact of gradient energy terms on the solute distribution and on the phase change in interstitial solutions with misfit and the absence of solid-state wetting there.

In its panels (a) and (c), Fig. 9 shows plateau chemical potentials and charging/discharging hysteresis in μ for scenarios where gradient energy is included but coherency constraints are ignored. Symbols represent the simulation. It is seen that the $\Delta\mu^{\mathrm{pla}}$ are only weakly shifted from their bulk value, 0. The $\Delta\mu^{\mathrm{hys}}$ also remain close to the values of the corresponding bulk scenarios, represented by lines. Obviously, size and inert layers have only a weak impact on the chemical potential's plateau and hysteresis values if coherency constraints are ignored.

The picture changes when coherency constraints—that is, the mechanical interaction between the bulk and coherent inert layers—are accounted for. Panel (b) in Fig. 9 shows the strong downward shift of $\Delta\mu^{\mathrm{pla}}$ for the associated scenarios. The shift increases with decreasing sample thickness. What is more, Fig. 9(d) shows that the $\Delta\mu^{\mathrm{hys}}$ also decreases strongly relative to the corresponding bulk graph, which is the gray straight line in the figure. Instead, the data for both layer thicknesses are in excellent agreement with Eq. (32), the colored curved lines.

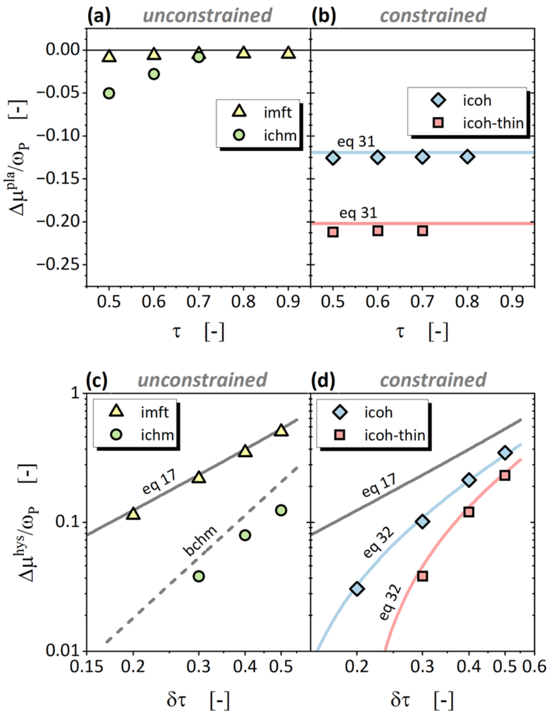

FIG. 9. Summarizing the impact of the scenarios on the chemical potential plateau and hysteresis values, μ^{pla} [(a) and (b)] and $\Delta\mu^{hys}$ [(c) and (d); on log–log scales], respectively. Chemical potentials are shown normalized to the total solute–solute interaction parameter, ω_P, and plotted vs reduced temperature parameters τ or $\delta\tau = 1 - \tau$. Left column of graphs: Scenarios ignoring coherency constraints; right column: scenarios accounting for constraints. All scenarios account for gradient energy contributions and, therefore, include conceivable wetting phenomena. Note that scenario ichm, with chemical interaction only, is not realistic for interstitial solutions. Realistic scenarios have a noticeable shift in plateau value and a noticeable deviation of hysteresis from bulk behavior [gray solid line, Eq. (17)] only when coherency constraints are accounted for. Colored solid lines: in (b), Eq. (31) for μ^{pla}; in (d), Eq. (32) for μ^{hys}. Dashed line in (c): Fit to numerical model for bulk with chemical interactions only [scenario bchm, fit in Fig. 3(c)] for reference.

Summarizing this part of our study, scenarios accounting for misfit strain exhibit substantial shifts in plateau and hysteresis chemical potentials only when mechanical coherency constraints are accounted for. It is emphasized that scenario ichm—which displays thick wetting layers and noticeable shifts of μ^{plat} and μ^{hys} without coherency strain—is not a natural representation of interstitial solid solutions, as it ignores the misfit strain that is inherent in their atomic structure.

V. DISCUSSION

We have studied the coherent phase change in finite-size interstitial solutions, with an eye on the relative importance of critical point wetting and coherency stress. We have allowed for surface layers that are strongly enriched in solute, biasing the bulk toward the concentrated phase. Composition-gradient energy terms and/or elasticity provide for nonlocal interaction by which the surfaces interact with the bulk. Both interaction mechanisms act in our numerical simulation.

Misfit strain, an inherent property of interstitial solutions, prompts an attractive solute–solute interaction (positive interaction parameter ω) and, hence, the trend for a miscibility gap. Based on Pd-H and $LiFeO_4$ as canonical examples, we work with a misfit contribution to ω that is twice as large as the contribution from chemical bonds; in other words, we take a misfit strength parameter value $\mathbb{Q} \approx 2/3$ as exemplary for interstitial solutions. For reference, we also inspect solutions with no misfit and exclusively chemical interaction; hence $\mathbb{Q} = 0$.

With $\mathbb{Q} = 0$, we find only moderate downward shifts in the plateau chemical potential μ^{pla} and in the charging/discharging hysteresis $\Delta\mu^{hys}$, yet a substantial decrease in the upper consolute temperature T^C and a strong (up to several dense-packed crystal monolayers, ML) Gibbs excess, Γ, in solute at the surface. Γ increases as T^C is approached, and this increase eventually initiates the phase transformation. The large Γ may be understood with reference to the theory of critical point wetting.[30] Yet, our study resolves no first-order wetting transition.

With $\mathbb{Q} \approx 2/3$, we find that Γ never exceeds a small fraction of 1 ML; in other words, wetting can be disregarded in our canonical interstitial solutions. However, finite-size and surface effects here shift μ^{pla} quite noticeably to negative, increasingly so as the system size decreases. The bulk solution with $\mathbb{Q} \approx 2/3$ has a larger $\Delta\mu^{hys}$ than the bulk $\mathbb{Q} = 0$ one. In small systems with misfit, however, the coherency stress reduces $\Delta\mu^{hys}$ substantially. Equally pronounced is the coherency-induced decrease, at small size, in T^C. We emphasize that the findings can be unequivocally identified as consequences of the coherency stress and not as wetting related: when the coherency stress is switched off while the layer-bulk coupling by gradient energy is maintained, we find that the size-dependent effects diminish drastically.

With attention to solutions with strong misfit, we present equations for the contribution of coherency stress to the size dependence of T^C, μ^{pla}, and $\Delta\mu^{hys}$. The materials' properties enter these relations exclusively through $\mathbb{Q}$. The coherency constraints are shown to (1) make the solute-solute interaction less attractive (less positive interaction parameter, ω) and to (2) make the matrix-solute interaction more attractive (negative shift in the plateau chemical potential, μ^{pla}). The simulation results agree well with that theory, yet T^C exhibits a small extra size-dependence due to nonlocal chemical interaction. That latter effect prevails even though $\Gamma \ll 1$ ML. In other words, the nonlocal chemical interaction is relevant even though no wetting layer is formed.

Our observations invite comparison to the theory in Ref. 27 for the impact of solid-state wetting. That theory has μ for the transformation onset shifting in proportion to the inverse system size and to the square-root of the Eshelby parameter. In other words, the theory predicts no shift when there is no misfit strain. This is not intuitively obvious, as one would expect the gradient energy to drive wetting, whereas the mechanical energy would act to stiffen the composition profile and, thereby, to oppose wetting. Consistent with that expectation, and contrary to the theory of Ref. 27, our results exhibit pronounced wetting layers only when there is no misfit strain.

Approaches to a continuum theory of critical point wetting rely on a gradient-square contribution to the free energy in the bulk, along with superficial boundary conditions that are derived from that contribution. Yet, as was shown by Cahn and Hilliard,[19] nonuniformity enters the energy of the Ising-type bond counting model—as it underlies our numerical analysis—inherently through the second derivative of the composition profile. Upon transforming the equations to the gradient-square form by partial integration, one generates a residuum that depends on ∇x at the surface.[19] Available continuum approaches to critical point wetting[27,30,60,61] do not include the superficial energy term corresponding to the residuum and so do not strictly apply to our scenarios. Furthermore, our simulation reveals discontinuous jumps in the composition at the interface between the bulk and the solute-rich superficial layers; these jumps are again not immediately accounted for in simple continuum analysis. For want of appropriate theory, our work restricts itself to a qualitative discussion of the observations concerning wetting.

We emphasize that the absence of misfit strain in the $\mathbb{Q} = 0$ scenarios makes them unrealistic as representations of interstitial solutions for energy storage. Thereby, the size dependence of the phase change in realistic representations is controlled by coherency strain contributions and not by wetting.

At the heart of the suppression of wetting in misfit-dominated solid solutions is the weakness of their Cahn–Hilliard gradient energy constant κ. As κ is commonly taken to scale with chemical (ω_{chm}) as opposed to mechanical interaction strength (ω_{mft}), κ is small in solutions with large $\mathbb{Q}$.[62,63] Then, composition-gradient energy may not achieve efficient coupling between solute-enriched layers and the bulk. In our simulation, this is confirmed when comparing the Γ for our ichm ($\mathbb{Q} = 0$) and imft ($\mathbb{Q} \approx 2/3$) scenarios: the first has Γ reach up to 8 ML, whereas the second provides the maximum value of 0.1 ML, or 80 times less.

Linear continuum elasticity does not provide for gradient-square terms, supporting the scaling between κ and ω_{chm}, not ω_{mft}. By contrast, the microscopic lattice-based elasticity theory of Ref. 62 does suggest a misfit-related contribution to κ. Yet, that contribution is negligible unless the concentration-strain coupling coefficient exceeds $\eta = 0.1$.[64] Our canonical examples remain well below that value.

Our study contributes to identifying the mechanism through which the small size and the surfaces affect the conditions for phase change in interstitial solid solution nanoparticles for energy storage, and it presents equations for the impact of the size on the upper consolute temperature of the miscibility gap, the plateau chemical potential, and the charging/discharging hysteresis. Those parameters provide metrics that are of immediate relevance for the performance of energy storage materials, since they contribute to determining practicable temperature domains, voltage or pressure values for stable operation, and energy dissipation during charging/discharging. Clarifying their size dependence may contribute to a rational design of energy storage schemes.

SUPPLEMENTARY MATERIAL

The supplementary material provides the following items, concatenated in a single PDF file: S1—exemplary materials parameters for (Li)$FePO_4$; S2—details of the numerical implementation, and specifically its use of dimensionless units; S3—results of the supporting study of a hypothetical scenario with coherency stress but no cross-interface bonds.

ACKNOWLEDGMENTS

We acknowledge Professor. Karsten Albe for a critical reading and the German Research Foundation (DFG) for funding through Grant No. WE1424/18-1.

AUTHOR DECLARATIONS

Conflict of Interest

The authors have no conflicts to disclose.

Author Contributions

Yong Li: Conceptualization (equal); Formal analysis (supporting); Investigation (equal); Methodology (lead); Validation (equal); Writing – original draft (equal); Writing – review & editing (equal). **Jörg Weissmüller**: Conceptualization (equal); Formal analysis (lead); Funding acquisition (lead); Investigation (equal); Methodology (supporting); Validation (equal); Writing – original draft (equal); Writing – review & editing (equal).

DATA AVAILABILITY

The data that support the findings of this study are available from the corresponding author upon reasonable request.

REFERENCES

[1] J. Bellosta von Colbe, J.-R. Ares, J. Barale, M. Baricco, C. Buckley, G. Capurso, N. Gallandat, D. M. Grant, M. N. Guzik, I. Jacob, E. H. Jensen, T. Jensen, J. Jepsen, T. Klassen, M. V. Lototskyy, K. Manickam, A. Montone, J. Puszkiel, S. Sartori, D. A. Sheppard, A. Stuart, G. Walker, C. J. Webb, H. Yang, V. Yartys, A. Züttel, and M. Dornheim, "Application of hydrides in hydrogen storage and compression: Achievements, outlook and perspectives," Int. J. Hydrogen Energy **44**(15), 7780–7808 (2019).

[2] A. Renuka Balakrishna, "Crystallographic design of intercalation materials," J. Electrochem. Energy Convers. Storage **19**(4), 040802 (2022).

[3] P. Fratzl, O. Penrose, and J. L. Lebowitz, "Modeling of phase separation in alloys with coherent elastic misfit," J. Stat. Phys. **95**(5–6), 1429–1503 (1999).

[4] R. B. Schwarz and A. G. Khachaturyan, "Thermodynamics of open two-phase systems with coherent interfaces," Phys. Rev. Lett. **74**(13), 2523–2526 (1995).

[5] D. B. Ravnsbaek, K. Xiang, W. Xing, O. J. Borkiewicz, K. M. Wiaderek, P. Gionet, K. W. Chapman, P. J. Chupas, and Y. M. Chiang, "Extended solid solutions and coherent transformations in nanoscale olivine cathodes," Nano Lett. **14**(3), 1484–1491 (2014).

[6] J. Weissmüller and C. Lemier, "On the size dependence of the critical point of nanoscale interstitial solid solutions," Philos. Mag. Lett. **80**(6), 411–418 (2000).

[7] C. Sachs, A. Pundt, R. Kirchheim, M. Winter, M. T. Reetz, and D. Fritsch, "Solubility of hydrogen in single-sized palladium clusters," Phys. Rev. B **64**(7), 075408 (2001).

[8] N. Meethong, H.-Y. S. Huang, W. Carter, and Y.-M. Chiang, "Size-dependent lithium miscibility gap in nanoscale $Li_{1-x}FePO_4$," Electrochem. Solid-State Lett. **10**(5), A134 (2007).

[9] D. Burch and M. Z. Bazant, "Size-dependent spinodal and miscibility gaps for intercalation in nanoparticles," Nano Lett. **9**(11), 3795–3800 (2009).

[10] M. Tang, W. C. Carter, and Y.-M. Chiang, "Electrochemically driven phase transitions in insertion electrodes for lithium-ion batteries: Examples in lithium metal phosphate olivines," Annu. Rev. Mater. Res. **40**(1), 501–529 (2010).

[11] S. Wagner, H. Uchida, V. Burlaka, M. Vlach, M. Vlcek, F. Lukac, J. Cizek, C. Baehtz, A. Bell, and A. Pundt, "Achieving coherent phase transition in palladium–hydrogen thin films," Scr. Mater. **64**(10), 978–981 (2011).

[12] J. Pohl, C. Stahl, and K. Albe, "Size-dependent phase diagrams of metallic alloys: A Monte Carlo simulation study on order–disorder transitions in Pt–Rh nanoparticles," Beilstein J. Nanotechnol. **3**, 1–11 (2012).

[13] R. Bardhan, L. O. Hedges, C. L. Pint, A. Javey, S. Whitelam, and J. J. Urban, "Uncovering the intrinsic size dependence of hydriding phase transformations in nanocrystals," Nat. Mater. **12**(10), 905–912 (2013).

[14] A. Baldi, T. C. Narayan, A. L. Koh, and J. A. Dionne, "In situ detection of hydrogen-induced phase transitions in individual palladium nanocrystals," Nat. Mater. **13**(12), 1143–1148 (2014).

[15] R. Griessen, N. Strohfeldt, and H. Giessen, "Thermodynamics of the hybrid interaction of hydrogen with palladium nanoparticles," Nat. Mater. **15**(3), 311–317 (2016).

[16] S. Wagner and A. Pundt, "Quasi-thermodynamic model on hydride formation in palladium–hydrogen thin films: Impact of elastic and microstructural constraints," Int. J. Hydrogen Energy **41**(4), 2727–2738 (2016).

[17] R. Spatschek, G. Gobbi, C. Hüter, A. Chakrabarty, U. Aydin, S. Brinckmann, and J. Neugebauer, "Scale bridging description of coherent phase equilibria in the presence of surfaces and interfaces," Phys. Rev. B **94**(13), 134106 (2016).

[18] J. Weissmüller, "Coherent phase change in interstitial solutions: A hierarchy of instabilities," Adv. Sci. **11**, 2308554 (2024).

[19] J. W. Cahn and J. E. Hilliard, "Free energy of a nonuniform system. I. Interfacial free energy," J. Chem. Phys. **28**(2), 258–267 (1958).

[20] J. W. Cahn, "On spinodal decomposition," Acta Metall. **9**(9), 795–801 (1961).

[21] Z.-K. Liu and J. Ågren, "On two-phase coherent equilibrium in binary alloys," Acta Metall. Mater. **38**(4), 561–572 (1990).

[22] P. W. Voorhees and W. C. Johnson, "The thermodynamics of elastically stressed crystals," in *Solid State Physics*, edited by H. Ehrenreich and F. Spaepen (Academic Press, 2004), Vol. 59, pp. 1–201.

[23] J. M. Rahm, J. Löfgren, and P. Erhart, "Quantitative predictions of thermodynamic hysteresis: Temperature-dependent character of the phase transition in Pd–H," Acta Mater. **227**, 117697 (2022).

[24] J. Tretkowski, J. Völkl, and G. Alefeld, "Sample-shape dependence of the spinodals and the diffusion coefficients for hydrogen in niobium and tantalum," Z. Phys. B: Condens. Matter **28**(4), 259–264 (1977).

[25] H. Zabel and H. Peisl, "Coherent α–α′ phase transition of hydrogen in niobium," Acta Metall. **28**(5), 589–599 (1980).

[26] G. Jerkiewicz, "Electrochemical hydrogen adsorption and absorption. Part 1: Under-potential deposition of hydrogen," Electrocatalysis **1**(4), 179–199 (2010).

[27] D. A. Cogswell and M. Z. Bazant, "Theory of coherent nucleation in phase-separating nanoparticles," Nano Lett. **13**(7), 3036–3041 (2013).

[28] M. Tang, H. Y. Huang, N. Meethong, Y. H. Kao, W. C. Carter, and Y. M. Chiang, "Model for the particle size, overpotential, and strain dependence of phase transition pathways in storage electrodes: Application to nanoscale olivines," Chem. Mater. **21**(8), 1557–1571 (2009).

[29] M. Tang, J. F. Belak, and M. R. Dorr, "Anisotropic phase boundary morphology in nanoscale olivine electrode particles," J. Phys. Chem. C **115**(11), 4922–4926 (2011).

[30] J. W. Cahn, "Critical point wetting," J. Chem. Phys. **66**(8), 3667–3672 (1977).

[31] M. J. Welland, D. Karpeyev, D. T. O'Connor, and O. Heinonen, "Miscibility gap closure, interface morphology, and phase microstructure of 3D $\mathrm{Li}_x\mathrm{FePO}_4$ nanoparticles from surface wetting and coherency strain," ACS Nano **9**(10), 9757–9771 (2015).

[32] N. Meethong, H. Y. S. Huang, S. Speakman, W. C. Carter, and Y. M. Chiang, "Strain accommodation during phase transformations in olivine-based cathodes as a materials selection criterion for high-power rechargeable batteries," Adv. Funct. Mater. **17**(7), 1115–1123 (2007).

[33] L. Q. Chen, "On the elastic field coupling in the diffuse-interface modeling of coherent microstructures," in *Phase Transformations and Evolution in Materials as Held at the 2000 TMS Annual Meeting* (TMS, 2000), pp. 209–220.

[34] J. Christian, *The Theory of Transformations in Metals and Alloys*, 2nd ed. (Pergamon, Amsterdam, 2002).

[35] The original result, Eq. (3.8) in Ref. 19, is derived by counting bonds originating at "A" type atoms only for an A-B solution. Our Eq. (4) corrects that scheme by accounting also for the energy contributed by "B" atoms at the origin. Contrary to the expression in Ref. 19, Eq. (4) is invariant under $\{x \to 1 - x, \nabla^2 x \to -\nabla^2 x\}$, as is required for the bond-counting model. The results for the gradient-square representation, and specifically for κ, are not affected.

[36] J. D. Eshelby, *The Continuum Theory of Lattice Defects* (Academic Press, 1956), Vol. 3, pp. 79–144.

[37] For distinction from physical quantities, functions are marked by a tilde.

[38] R. García, C. M. Bishop, and W. C. Carter, "Thermodynamically consistent variational principles with applications to electrically and magnetically active systems," Acta Mater. **52**(1), 11–21 (2004).

[39] A. Dyck, T. Böhlke, A. Pundt, and S. Wagner, "Phase transformation in the palladium hydrogen system: Effects of boundary conditions on phase stabilities," Scr. Mater. **247**, 116117 (2024).

[40] C. Lemier and J. Weissmüller, "Grain boundary segregation, stress and stretch: Effects on hydrogen absorption in nanocrystalline palladium," Acta Mater. **55**(4), 1241–1254 (2007).

[41] J. W. Cahn, *Thermodynamics of Solid and Fluid Surfaces* (ASM, Metals Park, Ohio, 1978), pp. 3–23.

[42] J. Weissmüller and J. W. Cahn, "Mean stresses in microstructures due to interface stresses: A generalization of a capillary equation for solids," Acta Mater. **45**(5), 1899–1906 (1997).

[43] E. Wicke, H. Brodowsky, and H. Züchner, "Hydrogen in palladium and palladium alloys," in *Hydrogen in Metals II*, edited by J. Alefeld and G. Völkl (Springer, Berlin, Heidelberg, 1978), Vol. 29, pp. 73–155.

[44] T. B. Flanagan and W. Oates, "The palladium-hydrogen system," Annu. Rev. Mater. Sci. **21**(1), 269–304 (1991).

[45] J. W. Arblaster, "Crystallographic properties of palladium," Platinum Met. Rev. **56**(3), 181–189 (2012).

[46] H. Frieske and E. Wicke, "Magnetic susceptibility and equilibrium diagram of PdH_n," Ber. Bunsengesellschaft Phys. Chem. **77**(1), 48–52 (1973).

[47] T. B. Massalski, H. Okamoto, P. R. Subramanian, and L. Kacprzak, *Binary Alloy Phase Diagrams* (ASM International, Materials Park, OH, 1990).

[48] E. Brandes and G. Brook, *Smithells Metals Reference Book* (Elsevier, Butterworth-Heinemann, Oxford, 2013).

[49] H. Peisl, "Lattice strains due to hydrogen in metals," in *Hydrogen in Metals I*, edited by G. Alefeld and J. Völkl (Springer, Berlin, Heidelberg, 1978), Vol. 28, pp. 53–74.

[50] S. Shi, J. Markmann, and J. Weissmüller, "Actuation by hydrogen electrosorption in hierarchical nanoporous palladium," Philos. Mag. **97**, 1571–1587 (2017).

[51] The survey in Ref. 49 shows the relative volume expansion of per H in Pd-H as $\Delta V/V = 0.19$, from which one may infer $\eta = (1.19)^{1/3} - 1 = 0.060$ for concentrated solutions. This agrees with $\eta = 0.060 \pm 0.002$ from a recent dilatometry study.[50] From a dilute solution perspective, the data in Ref. 49 imply $\eta = 0.19/3 = 0.063$. The conclusions in the present work are not affected by the difference.

[52] P. Fratzl and O. Penrose, "Ising model for phase separation in alloys with anisotropic elastic interaction—I. Theory," Acta Metall. Mater. **43**(8), 2921–2930 (1995).

[53] T. Mütschele and R. Kirchheim, "Hydrogen as a probe for the average thickness of a grain boundary," Scr. Metall. **21**(8), 1101–1104 (1987).

[54] D. Frenkel and B. Smit, *Understanding Molecular Simulation: From Algorithms to Applications* (Elsevier, 2002).

[55] M. P. Allen and D. J. Tildesley, *Computer Simulation of Liquids* (Oxford University Press, 2017).

[56] T. Krekeler, A. V. Straßer, M. Graf, K. Wang, C. Hartig, M. Ritter, and J. Weissmüller, "Silver-rich clusters in nanoporous gold," Mater. Res. Lett.**5**, 314–321 (2017).

[57] Y. Li, B.-N. Ngo-Dinh, J. Markmann, and J. Weissmüller, "Evolution of length scales and of chemical heterogeneity during primary and secondary dealloying," Acta Mater. **222**, 117424 (2022).

[58] G. Henkelmann, D. Waldow, M. Liu, L. Lührs, Y. Li, and J. Weissmüller, "Self-detachment and subsurface densification of dealloyed nanoporous thin films," Nano Lett. **22**(16), 6787–6793 (2022).

[59] In transferring the result for the event probability from (Ref. 55, Sec. 4.7) to the present problem, we introduced the factor $\mathcal{N}_{\mathrm{A}}^{-1}$ to obtain a per-particle chemical potential based on μ in our per-mole notation, and we accounted for the fact that the swap is here between solute and a vacancy at chemical potential 0.

[60] D. Bonn and D. Ross, "Wetting transitions," Rep. Prog. Phys. **64**(9), 1085–1163 (2001).

[61] B. M. Law, "Wetting, adsorption and surface critical phenomena," Prog. Surf. Sci. **66**(6–8), 159–216 (2001).

[62] H. E. Cook and D. de Fontaine, "On the elastic free energy of solid solutions—I. Microscopic theory," Acta Metall. **17**(7), 915–924 (1969).

[63] S. Y. Hu and L. Q. Chen, "Solute segregation and coherent nucleation and growth near a dislocation—A phase-field model integrating defect and phase microstructures," Acta Metall. **49**(3), 463–472 (2001).

[64] H. E. Cook and D. De Fontaine, "On the elastic free energy of solid solutions—II. Influence of the effective modulus on precipitation from solution and the order-disorder reaction," Acta Metall. **19**(7), 607–616 (1971).